JOURNAL OF MATERIALS SCIENCE 37 (2002) 3521 – 3532

Influence of directional solidification variables on the cellular and primary dendrite arm spacings of PWA1484

L. LI, R. A. OVERFELT
Mechanical Engineering Department, Auburn University,
201 Ross Hall, Auburn, AL 36849, USA
E-mail: overfra@auburn.edu

A series of directional solidification experiments have been performed to elucidate the effects of thermal gradient G and growth velocity V on the solidification behavior and microstructural development of the multicomponent Ni-base superalloy PWA 1484. A range of aligned as-cast microstructures were exhibited by the alloy: (i) aligned dendrites with well developed secondary and tertiary arms; (ii) flanged cellular dendrites aligned with the growth direction and without secondary arms; and (iii) cells with no evidence of flanges or secondary arms. The role of the imposed process parameters on the primary arm spacings that developed in the Bridgman-grown samples were examined in terms of current theoretical models. The presence of secondary arms increases the spacings between dendrites and leads to a greater sensitivity of λ_1 on $G^{-1/2}\ V^{-1/4}$. The exponent of V was analyzed and found to depend upon the imposed gradient G. High withdrawal velocities and low thermal gradients were found to cause radial non-uniformity of the primary dendrite arm spacing. Such behavior was associated with off-axis heat flows.

1. Introduction

The columnar arm spacings of directionally solidified materials are very important microstructural features that impact basic transport phenomena in the mushy zone and the subsequent mechanical properties of cast products. The dendrite arm spacings and morphology directly influence convection in the mushy zone and dominate the occurrence of grain defects, freckle/channel segregates and porosity in the microstructure [1–3]. Thus the variation of primary dendrite arm spacings during directional solidification has been extensively studied [4–10]. Although much of the fundamental phenomena of microstructural development and transition (i.e., planar interface → cells → dendrites → equiaxed grains) are qualitatively understood, there remains considerable work to quantitatively describe multi-component systems, growth with mis-aligned thermal fields, and growth during transient thermal conditions.

Hun [11] developed the first theoretical formulation to predict dendrite arm spacings based upon the imposed process parameters. In Hunt's model, several assumptions were invoked to simplify the treatment: (1) The thermal and compositional gradients in the direction parallel to the growth direction are constant; (2) The tip of the dendrite or cell is a steady parabolic shape; and (3) The cell or dendrite grows at the minimum undercooling for a given growth velocity. Hunt's initial theoretical model resulted in a relationship of the form:

$$\lambda_1 = \left\{ 2.83\left(\frac{\gamma D}{\Delta S}\right)^{1/4} \left[m(1-k)C_0 + \frac{kGD}{V} \right]^{1/4} \right\} \times G^{-1/2} V^{-1/4} \tag{1}$$

The first term in the braces is primarily a combination of material constants for a given alloy. γ is the alloy solid–liquid interfacial energy, D is the solute diffusion coefficient, ΔS is the entropy of fusion per unit volume, m is the slope of the liquidus, k is the solute distribution coefficient and C_0 is the alloy composition. G and V are the longitudinal thermal gradient and growth velocity at the aligned dendrite tip, respectively.

Subsequently Kurz and Fisher [12] published a modified theoretical model utilizing the stability criterion proposed by Langer and Muller-Krumbhaar [13]. In addition, Kurz and Fisher assumed the tips of the cells/dendrites were smooth ellipsoids and the cells/dendrites form uniform hexagon arrays. Thus, Kurz and Fisher obtained the following results for cells and dendrites:

$$\text{Cells:}\quad \lambda_1 = \left[\frac{6\Delta T'}{G(1-k)}\right]^{1/2} \left[\frac{D}{V} - \frac{k\Delta T_0}{G}\right]^{1/2} \tag{2}$$

0022–2461

Dendrites:

$$\lambda_1 = 4.3\left\{\Delta T'^2 \frac{\Gamma D}{k\Delta T_0}\right\}^{1/4} G^{-1/2} V^{-1/4} \tag{3}$$

where Γ is the Gibbs-Thomson coefficient ($=\gamma/\Delta S$) and $\Delta T'$ and ΔT_0 are the non-equilibrium and equilibrium freezing ranges, respectively. As in Hunt's previous model, the first term in the braces for dendrites is an alloy dependent constant. For dendritic growth, even though Hunt and Kurz and Fisher applied different arguments, similar expressions for dendritic growth were obtained. In fact, the only difference was in the derived alloy dependent constants.

Although overly simplistic, these two analytical models provide significant insight into the growth mechanisms and qualitative agreement with experimental data. Research continues to refine the models and extend their applicability. Hunt and Lu [14, 15] reported predictions of spacing from time dependent finite-difference models of solute transport during array growth of cells and dendrites. Fully self-consistent solutions were produced for axisymmetric interface shapes for well aligned growth conditions. The analytical relationships of the results of the numerical models are:

$$\text{Dendrites:}\quad \lambda_1 = 0.156(\Gamma k)^{a_d+0.4} D^{-a_d} \Delta T_0^{-a_d+0.2} \times \left(1 - \frac{V_c}{V}\right)^{3/4} G^{-0.6} V^{a_d} \tag{4}$$

where

$$a_d = -1.131 - 0.1555 \log_{10}\left(\frac{G\Gamma k}{\Delta T_0^2}\right) - 0.7589 \times 10^{-2}\left[\log_{10}\left(\frac{G\Gamma k}{\Delta T_0^2}\right)\right]^2 \tag{5}$$

$$\text{Cells:}\quad \lambda_c = 8.18k^{-0.335}\left(\frac{\Gamma}{mC_0(k-1)}\right)^{0.41}\left(\frac{D}{V}\right)^{0.59} \tag{6}$$

where V_c is the critical velocity where the interface will break down from a planar to a cellular structure and a_d is a gradient dependent exponential factor. An important feature of the numerical approach is that the spacing selection mechanism was incorporated into the model and no *a priori* assumptions were required (marginal stability, minimum undercooling, etc.). The critical spacing was considered to be achieved when the composition along the cell groove was nearest in composition to the equilibrium composition line. A principal result was that a constant spacing could exist over the range between the array stability limit (due to overgrowth) and the upper spacings limit (due to tip splitting or tertiary arm growth). The latter is twice the value of the former. Although the model was originally established for cells, it was extended to dendritic growth when it appeared to also provide reasonable predictions for dendritic structures.

Recently, Ma and Sahm [16] proposed a new analytic model to explain the variation in primary arm spacing with growth velocity and specifically included the effects of secondary arm growth on primary dendrite arm spacing. Ma and Sahm's analysis concluded that:

$$\lambda_1 = 2\pi(kD\Gamma\Delta T_0)^{1/4}\left(1 - \frac{V_c}{V}\right)^{3/4} G^{-1/2} V^{-1/4} \tag{7}$$

In this model, dendritic growth was resolved into 2 parts—growth of the dendritic center core and growth of the side arms. The arm spacings were considered to be the sum of the dendrite core diameter and twice the sidearm length. The dendritic core diameter was directly related to the dendrite core tip radius R. The side arm length was determined by the local free growth time and growth velocity until the side arm encountered the neighboring side arms. The side arm tip radius was assumed to be equal to the primary tip radius and the side arm growth velocity was assumed to be equal to the primary growth velocity (for dendritic growth only). Transverse (i.e., radial) thermal gradients were assumed to be negligible. Ma and Sahm tested their model and the Hunt and Lu [14, 15] model against experimental data of λ vs. V for directionally solidified succinonitrile-0.35 wt. pct. acetone, SRR99 superalloy and Pb-Ti alloy and found that their model gave better agreement.

The ability of mushy zone microstructures to adjust to non-ideal (transient, mis-aligned, etc.) growth conditions is becoming of increasing interest. Han and Trivedi [4] investigated the primary dendrite spacing adjustment process in succinonitrile-acetone after sudden increases in velocity and proposed a new lateral adjustment mechanism. Eshelman [17] studied the variation in average cellular spacing with velocity and observed that there was a finite band of velocities in which both cellular or dendritic structures were stable. Bouchard and Kirkaldy [8] evaluated the applicability of steady-state theories of Hunt and Kurz and Fisher to the unsteady-regime. Su *et al.* [18, 19] found that although the primary and secondary dendrite arm spacings in Al-4.5 wt. pct. Cu quickly adjust to increases in imposed velocity, the compositional profiles adjusted more slowly. Growth when the dendrites are mis-aligned with the thermal gradient was examined in succinonitrile-water alloys by Grugel and Zhou [20]. The primary dendrite arm spacings were measured as a function of growth velocity and orientation angle with respect to the applied temperature gradient. The spacings were found to increase with the angle from 0° to 45° at constant composition, growth velocity and thermal gradient G. Grugel and Zhou postulated that the increase in primary spacing was due to an increase in side arm growth velocity from the off-axis thermal gradients.

While the effects of V and G on primary arm spacings have been extensively investigated with simple binary alloys, experimental data on high melting point multi-component alloys, particularly at very low thermal gradients consistent with production conditions, are limited. These present experiments were designed to investigate the cellular and dendritic solidification behavior of the multicomponent Ni-base superalloy PWA 1484 over a wide range of imposed solidification velocities V and thermal gradients G.

2. Experimental procedures

Cylindrical bars of PWA 1484 with 1.9 cm diameter and 20 cm length were directionally solidified by Howmet Corp., Whitehall, MI. The composition of the PWA 1484 alloy utilized is listed in Table I. All sample bars were then remelted and solidified in a vertical Bridgman-type furnace apparatus at Auburn University. The device features a hot zone at the top and cold zone at the bottom, divided by a thin layer of adiabatic insulation. The system is shown schematically in Fig. 1. The hot zone furnace is an ATS Model 3320 which can be monitored and controlled at constant temperature up to 1600°C. High thermal gradients were produced by a cold zone consisting of a water-cooled copper coil. Low thermal gradients were produced by a "cold" zone consisting of a custom booster furnace. Thus a wide range of thermal gradients could be obtained from 12 to ~105 K/cm.

Sample bars were contained in alumina crucibles within alumina retorts. B-type thermocouples were located at the center of the samples and shielded from the melt by alumina sheaths. The alumina retort tube was sealed at the bottom to enable evacuation followed by a purge of argon gas to minimize oxidation of the alloy at elevated temperatures. The sample, crucible and retort assembly were attached to a Parker Compumotor drive system that allowed precise control of sample withdrawal velocity via computer. All the alloy bars were remelted and soaked for atleast 60 min at the desired elevated temperature prior to initiating withdrawal and solidification. Withdrawal velocities varied between 0.00005 cm/sec to 0.01 cm/sec.

TABLE I PWA 1484 composition distribution data (Solidified at $V = 0.0005$ cm/sec. and $G = 40.6$ K/cm)

	Al	Cr	Co	Mo	Ta	W	Re	Ni
Bulk alloy	4.88	5.51	9.17	2.31	9.11	8.09	3.45	57.49
Dendritic trunk (core)	4.51	5.28	9.57	1.93	7.43	9.55	4.70	57.03
Interdendritic	5.07	5.65	9.07	2.24	10.39	7.39	2.58	57.61
K_e^i	0.92	0.96	1.04	0.84	0.82	1.18	1.36	
Gamma prime (γ')	6.74	2.01	6.42		18.62	3.63		62.58
Carbides (MC)					95.86			4.14

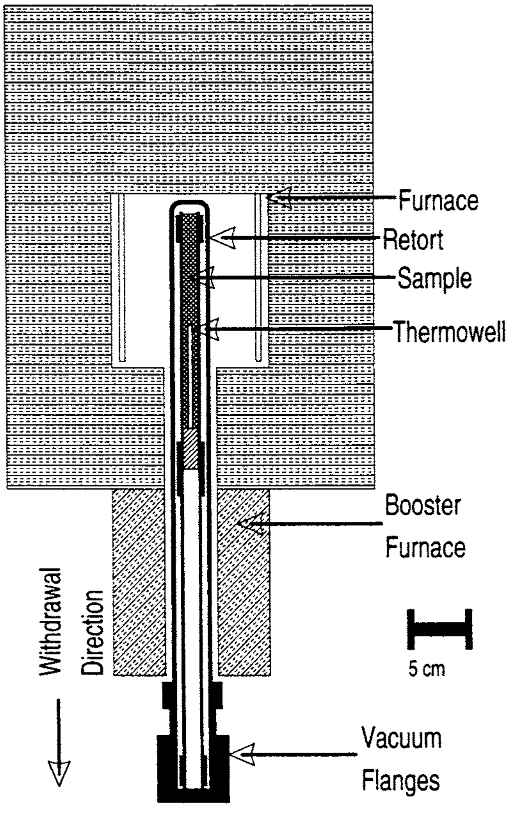

Figure 1 Schematic of the directional solidification apparatus.

The as-cast directionally solidified samples were lightly sanded and macro-etched to reveal the surface grain structure and any grain and/or segregation defects prior to sectioning for microstructural analyses. After macroetching, samples were sectioned at selected locations. Transverse sections, perpendicular to the growth direction, were cut from the middle of the samples. In this region dendrite arm spacing measurements are constant along the length indicating that steady state growth conditions were achieved. Longitudinal sections 2 cm long in the growth direction were also cut from the center of the cylindrical bar and immediately adjacent to the previously described transverse section. The sectioned pieces were mounted, ground and polished by standard metallographic techniques. All polished samples were etched for metallographic examination using a fresh solution of 10 ml HCl + 10 ml HNO_3 + molybdic acid 0.3 gm + 15 ml distilled water.

Metallographic examination was performed with an Olympus PME3 inverted metallurgical microscope. The transverse samples were used to determine the primary dendrite arm spacing λ_1, and longitudinal sections were used for the assessment of secondary dendrite arm spacing λ_2 . λ_1 was calculated by using the relationship $\lambda_1 = (A/N_1)^{0.5}$, where A is the area within which the number of dendrites N_1 was counted. λ_2 was calculated by using $\lambda_2 = N_2/L$, where L is the length of well-aligned dendritic trunks and N_2 is the number of secondary dendrite arms along the segment L.

Elemental distributions were measured by energy dispersive spectroscopy (EDS) in a JEOL 840 scanning electron microscope on transverse and longitudinal sections of a typical as-cast sample grown at $V = 0.0005$ cm/sec and $G = 40.6$ K/cm. Compositional analyses were performed on dendritic trunks, interdendritic regions, and secondary phases. The elemental microsegregation after solidification was evaluated by estimating a partition coefficient for each element (i) as $k_e^i = C_S^i / C_L^i$ where C_S^i is the composition of the element at the center of a dendrite trunk, and C_L^i is the solute element composition aof the bulk alloy.

3. Results and discussion

3.1. Directional solidification morphology

Figs 2 and 3 illustrate the microstructures observed in typical transverse and longitudinal sections of samples solidified over a range of velocities at a medium-high thermal gradient (41–108°C/cm) and at a low thermal gradient (12–40°C/cm), respectively. The growth velocities utilized are indicated on the figures and varies from 0.0005 to 0.01 cm/sec. The cells and dendrite cores exhibited excellent alignment with the axial

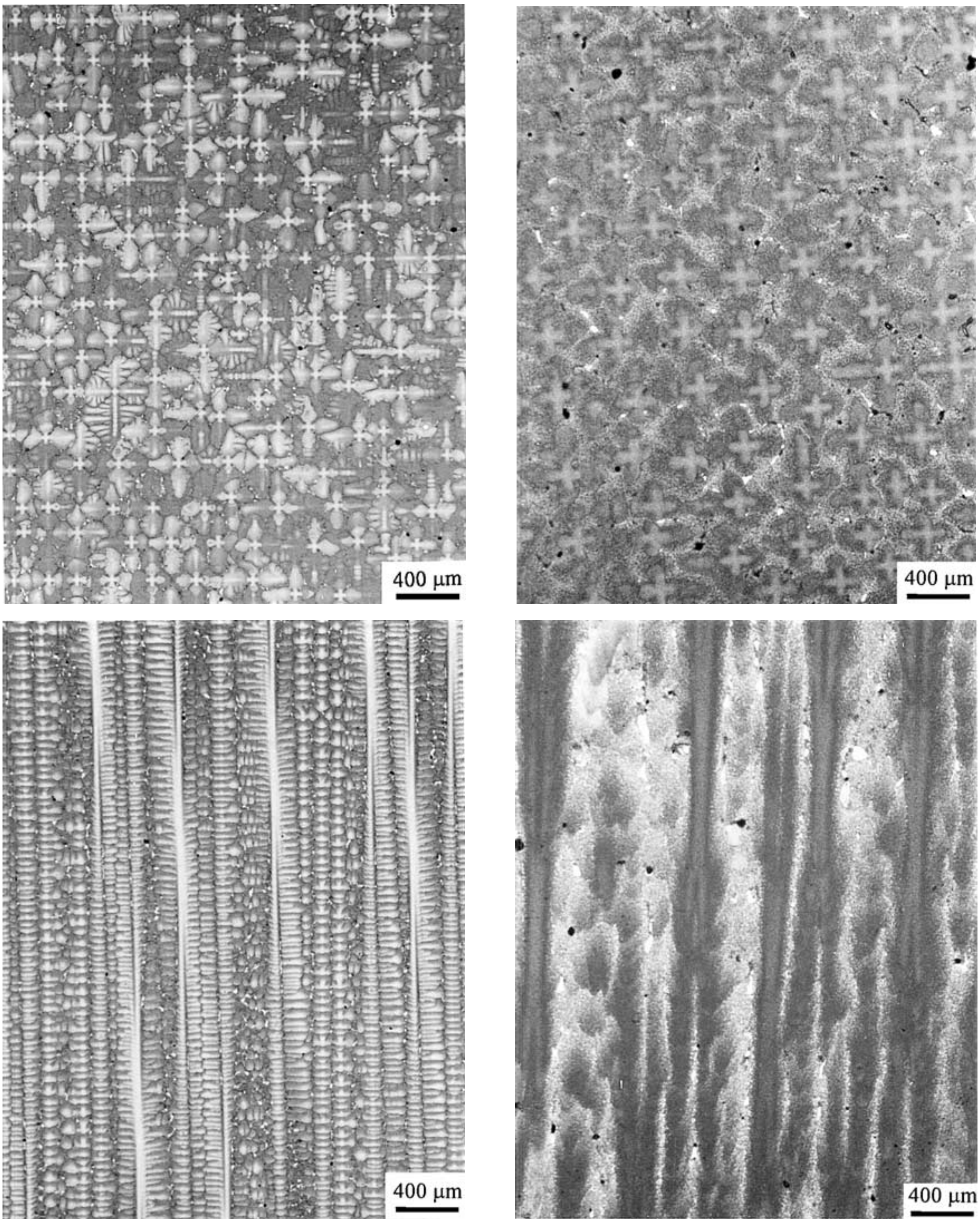

(a) G:105 K/cm; V:0.01 cm/sec

(b) G:88 K/cm; V:0.001 cm/sec

Figure 2 Typical microstructures of directionally solidified samples under high thermal gradients (54–105 K/cm) and a range of solidification velocities. Longitudinal thermal gradients (G) and solidification velocities (V) utilized are shown. Top: Tranverse sections; Bottom: Longitudinal sections. (*Continued.*)

thermal gradients imposed. The basic solidification microstructure of these samples is comprised of dendritic primary γ along with precipitates of γ' and metal carbides (MC) distributed throughout the interdendritic area. The average compositions of the various phases are listed in Table I.

The samples also displayed a transition from well-developed dendrites with tertiary arms (Figs 2a and 3a) to flanged cells (Figs 2c and 3c). (Some authors characterize the microstructures shown in Figs 2c and 3c as cellular dendrites.) The experimental velocities for transition from cellular-to-dendritic growth (V_t) can be difficult to evaluate as there is often inconsistency on the terminology employed in the literature. Cells grow without significant regard to the crystallographic orientation of the crystal structure. Some researchers prefer to describe a microstructure as dendritic only when secondary branches can be discerned in the as-cast microstructure, e.g., Flemings [21]. However, Kurz and Fisher [22] note that there is a range of intermediate forms (dendritic cells and cellular dendrites) when various degrees of crystallographic directionality

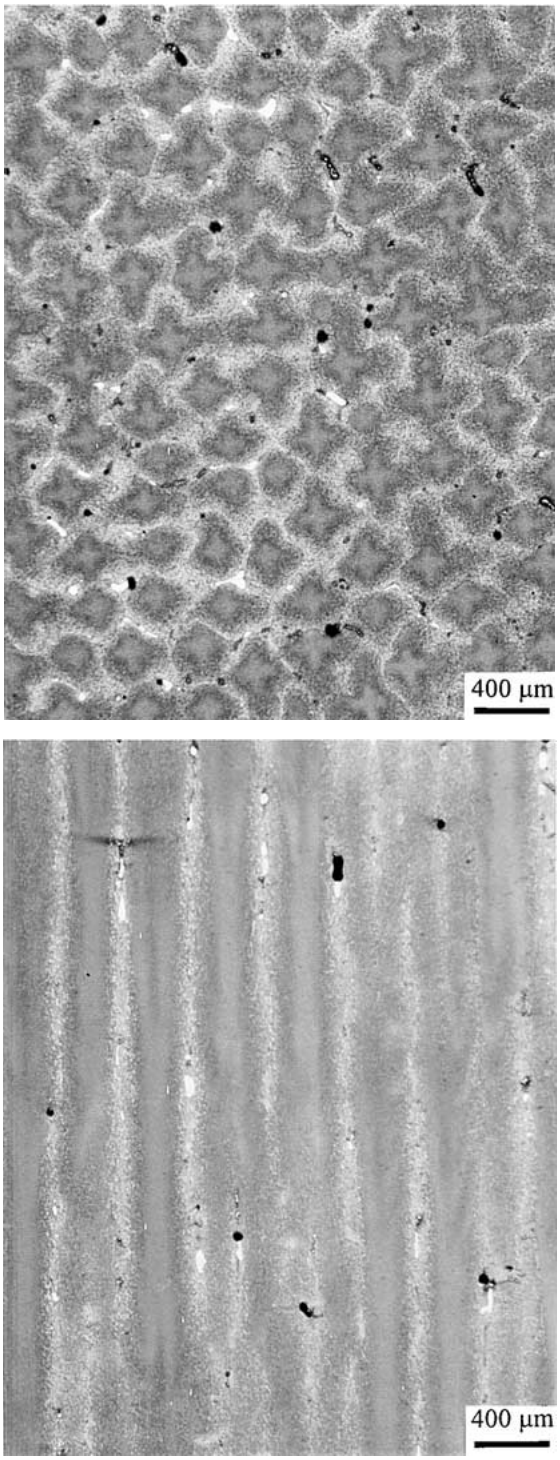

(c) G:54 K/cm; V:0.0005 cm/sec

Figure 2 (*Continued.*)

persist in the growth form even though no secondary arm development has occurred. The samples shown in Figs 2c and 3c exhibit microstructures where the underlying crystallographic orientation is evident in the primary arm and flange orientations, but no secondary dendrite arms were exhibited in the as-cast condition.

Samples were also grown at $V = 0.0001$ and 0.00005 cm/sec with $G = 40$ K/cm. Each sample was grown for approximately 6 cm and then quenched to preserve the mushy zone microstructure. Transverse and longitudinal sections of these samples are shown in Fig. 4. Examination of the cells near their tips in the longitudinal section shows evidence of secondary arms near some cell tips at growth velocities as low as 0.00005 cm/sec. These secondary arms were preserved from elimination by coarsening phenomena by the rapid cooling of the quenching process. Thus it appears that this sample is in transition from cellular to dendritic growth and V_t can be approximated as 0.00045 cm/sec. It also seems probable that the flanged cells shown in Figs 2c and 3c likely also exhibited secondary arms near their dendrite tips and that this morphology degenerated into the flanged cells seen at room temperature.

3.2. Primary dendritic and cellular arm spacings: λ_1

Fig. 5 illustrates the primary cell/arm spacings (λ_1) of PWA1484 correlated with the theoretical growth parameter $G^{-1/2}\ V^{-1/4}$. The velocities utilized and the morphology of each sample's microstructure at room temperature (cellular, flanged cellular, mixed cellular/dendritic, or dendritic) are identified by the symbols in Fig. 5. At the highest values of $G^{-1/2}$ $V^{-1/4}$, the samples exhibited cellular microstructures after cooling to room temperature. At the lowest values of $G^{-1/2}\ V^{-1/4}$, the samples exhibited well aligned dendritic microstructures with secondary arms. Intermediate values of $G^{-1/2}\ V^{-1/4}$ yielded samples which displayed mixed results. Intermediate values of $G^{-1/2}\ V^{-1/4}$ utilizing high velocities (e.g. 0.005 and 0.01 cm/sec and low gradients) produced dendritic microstructures. Intermediate values of $G^{-1/2}\ V^{-1/4}$ with a low velocity of 0.0005 cm/sec produced flanged-cellular microstructures. Intermediate values of $G^{-1/2}$ $V^{-1/4}$ with an intermediate velocity of 0.0025 cm/sec produced microstructures with mixed flanged-cellular and dendritic growth. The results of Fig. 5 show two distinct growth regimes: (1) Dendritic growth with a marked dependence of λ_1 on the theoretical parameter $G^{-1/2}\ V^{-1/4}$ and (2) Cellular growth with a much smaller dependence of λ_1 on $G^{-1/2}\ V^{-1/4}$.

Numerous experiments [8, 14, 23] have shown that the exponents of growth velocity V and thermal gradient G are often not simple constants of -0.25 and -0.5, respectively, but can vary with process conditions. Bouchard and Kirkaldy [8] summarized the relationships of primary arm spacing with G and V for various binary alloys in steady-state solidification and found a variation of the exponent for G from -0.37 to -0.54 and a variation of the exponent of V from -0.11 to -0.75. These researchers postulated that convective mixing might have cause such a wide variation. McCartney and Hunt [23] designed a neutrally buoyant Al-Mg-Si alloy so as to minimize gravity-induced convection in the liquid. Their directional solidification experiments yielded exponents of -0.55 and -0.28 for G and V, respectively, very close to the theoretical values.

In order to characterize the individual roles of V and G, as opposed to their coupled effects, the experimentally determined primary spacings are plotted versus V in Fig. 6. The gradients achieved in the samples are also shown in Fig. 6 and lines approximating constant G for 5 representative thermal gradients have been estimated and are included. As

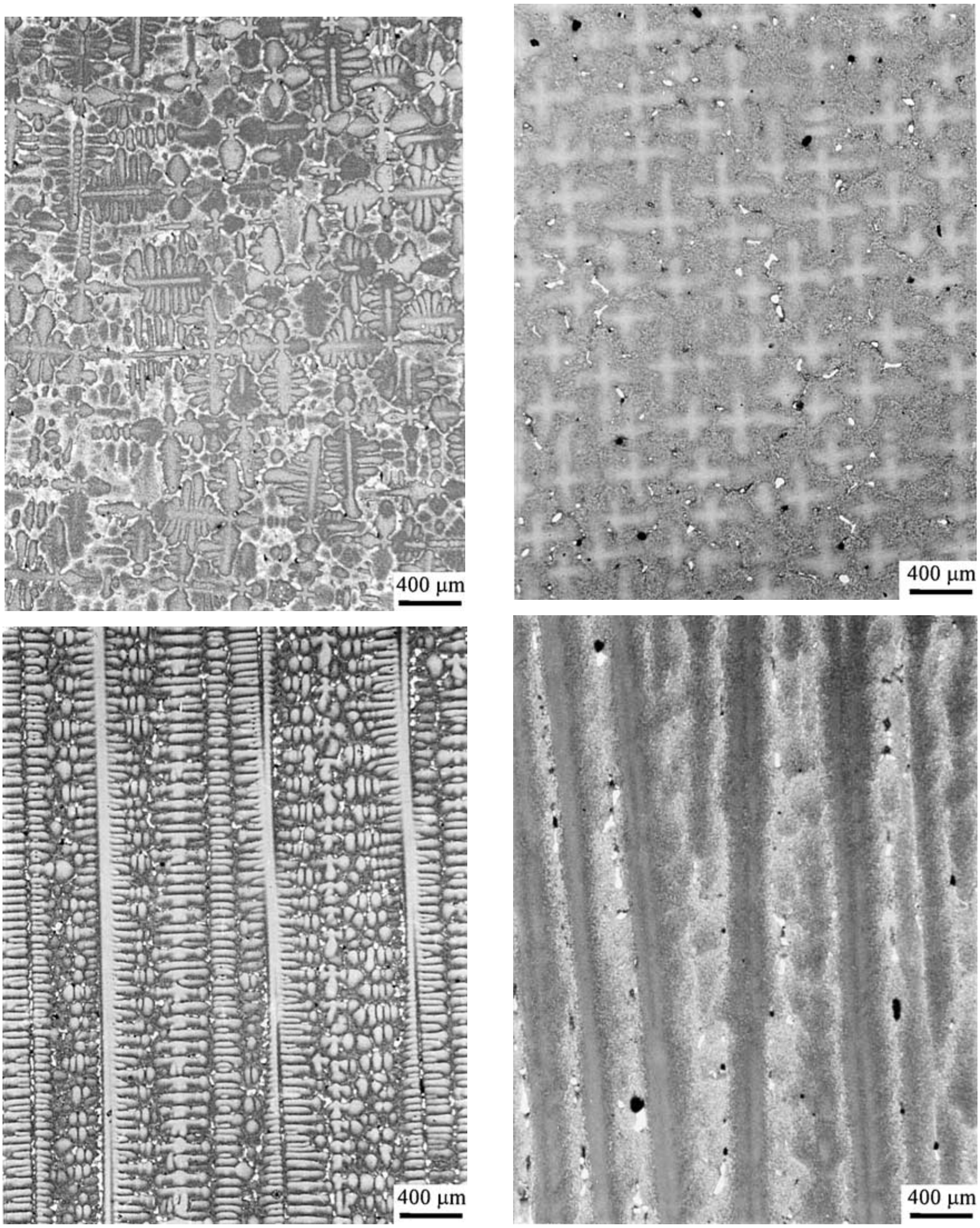

(a) G:17 K/cm; V:0.01 cm/sec

(b) G:23 K/cm; V:0.001 cm/sec

Figure 3 Typical microstructures of directionally solidified samples under low thermal gradients (17–25 K/cm) and a range of solidification velocities. Longitudinal thermal gradients (G) and solidification velocities (V) utilized are shown. Top: Tranverse sections; Bottom: Longitudinal sections. (*Continued.*)

noted before, dendritic microstructures were exhibited at $V > 0.001$ cm/sec while cellular-type microstructures were exhibited at $V < 0.001$ cm/sec. Gradient-dependent microstructures of cells or dendrites were seen at $V = 0.0025$–0.001 cm/sec. In addition, Fig. 6 shows that for all $G > 28$–$33°$C/cm, λ_1 decreases with increasing V, as expected. Fig. 6 also shows that the exponent of V decreases with decreasing thermal gradient G. This result is explicitly shown in Fig. 7. As the imposed thermal gradient increases, the exponent of V appears to be approaching the theoretical value of $a_d = -0.25$. Similar exponents of V were found under high gradient conditions by Kim [6] ($a_d = -0.17$) and Ma and Sahm [24] ($a_d = -0.19$).

The present primary spacing results were also compared to the earlier intuitive models of Hunt [11] and Kurz and Fisher [12] as well as the recent theoretical models proposed by Lu and Hunt [14, 15] and Ma and Sahm [16]. The physiochemical properties of PWA 1484 required for the theoretical analysis are shown in Table II. The constant effective partition coefficient k_e of the multi-component alloy was estimated using a

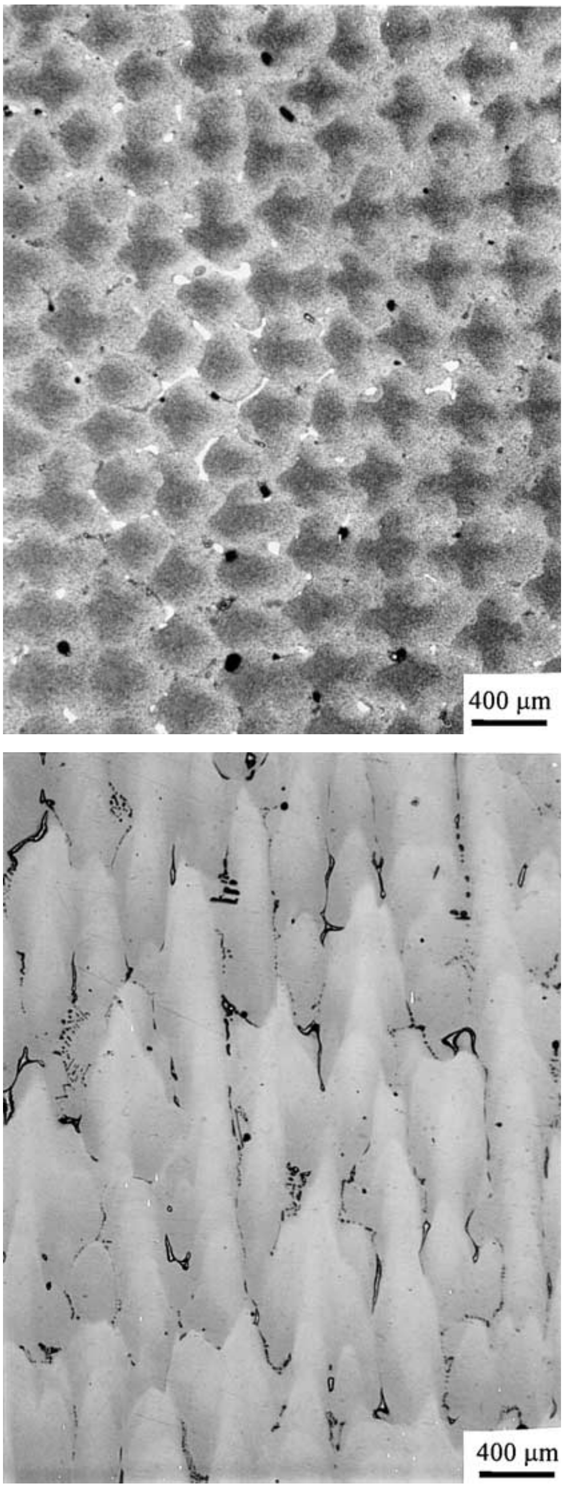

(c) G:25 K/cm; V:0.0005 cm/sec

Figure 3 (*Continued*.)

TABLE II Physiochemical data of PWA1484 used in the theoretical analysis

Parameter	Value
k_e	0.83
Γ (K cm)	1×10^{-5}
D (cm^2/s)	2×10^{-5}
$\Delta T'$ (K)	75
T' (K)	1668

modified Scheil equation [8], which was derived for a binary alloy with little solid state back-diffusion. A 2.5 cm long and 1.9 cm diameter sample of PWA1484 with a thermocouple inserted in the center was melted and frozen 6 times. The cooling curves obtained were evaluated by the method of Backerud [25] to identify the fraction solid f_s vs. temperature relationship. The maximum and minimum experimental curves thus obtained are shown in Fig. 8. The theoretical fraction solid vs. temperature relationship was also plotted in terms of equation [8], assuming that the liquidus and solidus are straight lines, *viz.*,

$$f_s = 1 - \left[\frac{T_m - T}{T_m - T_L}\right]^{1/k-1} \tag{8}$$

where T_m is the melting temperature of the pure element (i.e., 1453°C for Ni) and T_L is the liquidus temperature of the alloy. A pseudo-binary partition coefficient of $k_e = 0.83$ is seen in Fig. 8 to give good agreement with the observed solidification behavior. Such a pseudo-binary partition coefficient is in agreement with the elemental partition coefficients shown in Table I. In addition, the non-equilibrium freezing range of the alloy shown in Fig. 8 is 75 K. Differential scanning calorimetry experiments at low heating/cooling rates of 5°C/min indicated a freezing range of 80°C, consistent with that measured here. Following the methodology of previous investigators [6, 12, 24] ΔT_0 was assumed to be equal to $\Delta T'$ for the theoretical analyses shown below. The Gibbs-Thomson coefficient Γ is approximately 1×10^{-5} cm K for a number of alloys [22], and the mean diffusion coefficient D in the liquid is taken as 2×10^{-5} cm^2/s [16]. These values were utilized in the theoretical estimations below.

Fig. 9a–c compare the experimental primary dendrite arm spacing data with the theoretical models of Hunt [11], Kurz and Fisher [12] and Ma and Sahm [16] utilizing Equations 1, 3 and 7, respectively. Ma and Sahm's theory provided excellent prediction of both the primary dendrite arm spacing data as well as the dependence upon V under high gradients (Fig. 9a, $G \sim 100$ K/cm) and medium gradients (Fig. 9b, $G \sim 70$ K/cm). However, none of these theories satisfactorily explained the decreasing dependence of λ_1 on V at low thermal gradients.

The analytic expressions for cellular and dendritic spacings from Lu and Hunt's [14, 15] numerical results are plotted in Fig. 10. According to their model, the actual spacing for any condition could be any value between the array stability limit (a minimum value equal to equation [4]) and the upper spacing limit for either cells or dendrites. The upper spacing limit is typically twice the value of minimum array stability limit. In Fig. 10a (high thermal gradient) and (low thermal gradient), the hatched areas represent the available spacings for the given conditions. Good agreement is seen between the predictions of Lu and Hunt's model and the experimental data for conditions of dendritic growth at high thermal gradient. As before, poor agreement is exhibited by Lu and Hunt's model for the decreasing dependence of λ_1 on V at low thermal gradients.

It is well known that directional solidification microstructures transition from planar growth to cellular growth to dendrite growth as the velocity increases for the range of velocities considered here. Previous research [14, 15, 17, 24, 26] has shown that

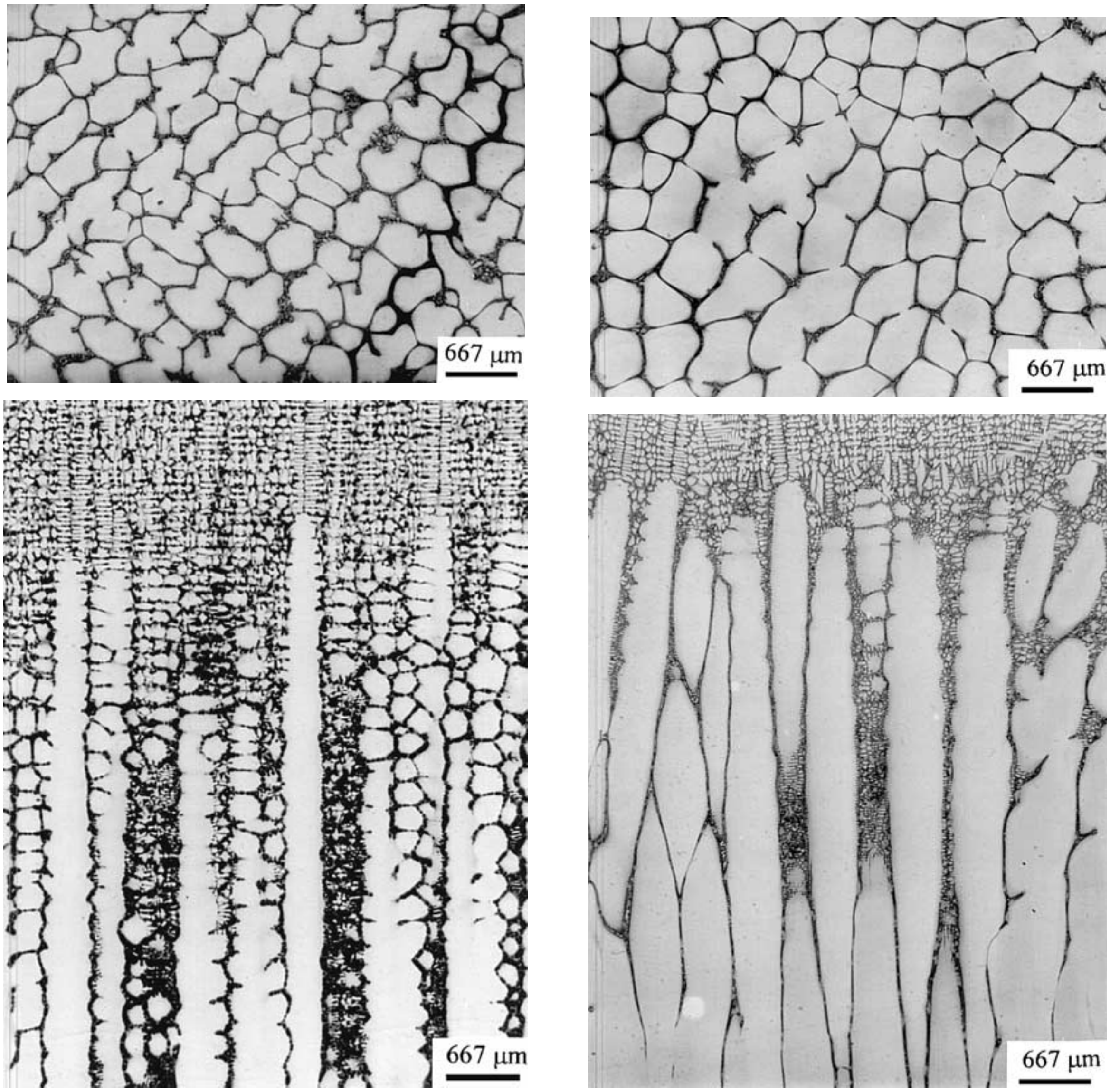

(a) (b)

Figure 4 Cellular microstructure of the quenched mushy zone of samples solidified at: (a) $V = 0.0001$ cm/sec and $G = 40$ K/cm; (b) $V = 0.00005$ cm/sec and $G = 40$ K/cm.

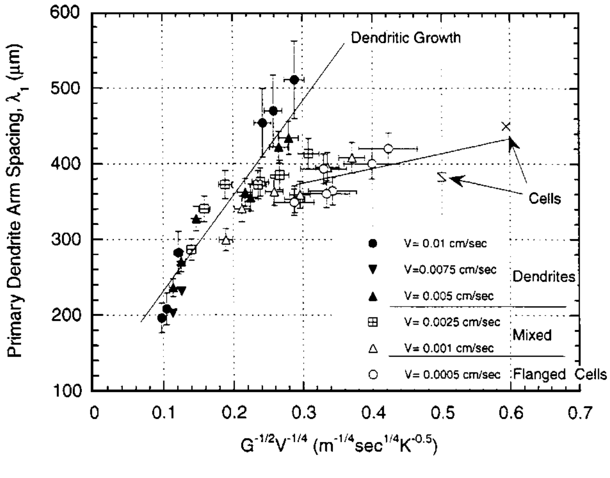

Figure 5 The primary arm spacings as a function of the solidification parameter $G^{-1/2}\ V^{-1/4}$. The velocities utilized and microstructures exhibited are shown.

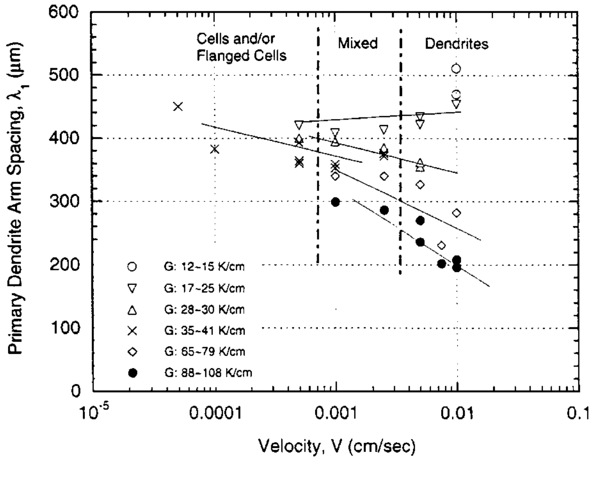

Figure 6 The primary arm spacings as functions of the solidification velocity for the range of thermal gradients shown. $G^{-1/2}\ V^{-1/4}$. The microstructures exhibited by the samples are also shown.

at intermediate ranges of velocity, cells and dendrites can co-exist and spacings are intermediate to those predicted for dendritic and cellular growth. McCartney and Hunt [23] reported a discontinuous range between dendrite and cell spacings for their neutrally buoyant Al-Mg-Si alloy directional solidification experiments. Lu and Hunt's numerical calculation [14, 15] also showed that two spacings solutions were possible at

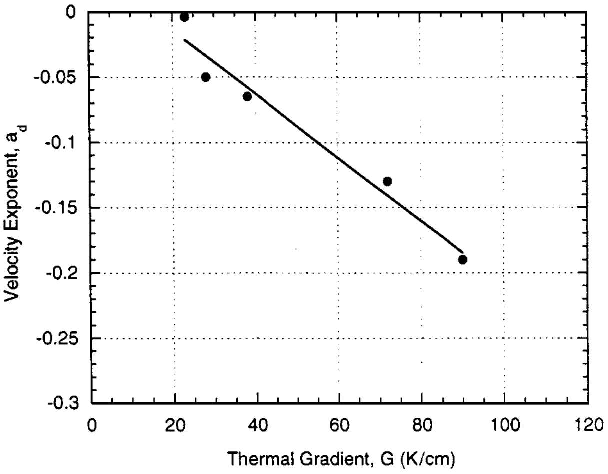

Figure 7 The dependence of the experimentally determined velocity exponent a_d with applied thermal gradient.

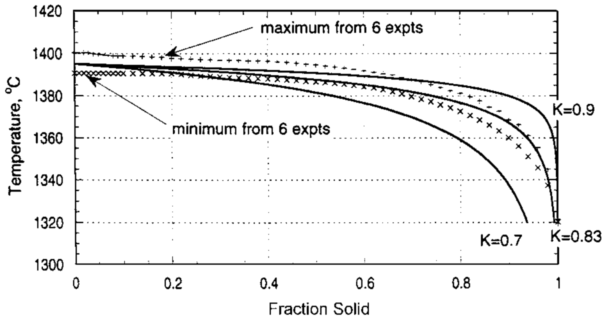

Figure 8 Temperature vs. fraction solid relationship for PWA1484. Minimum and maximum of a sample melted and frozen 6 times as well as estimates using Scheil's equation.

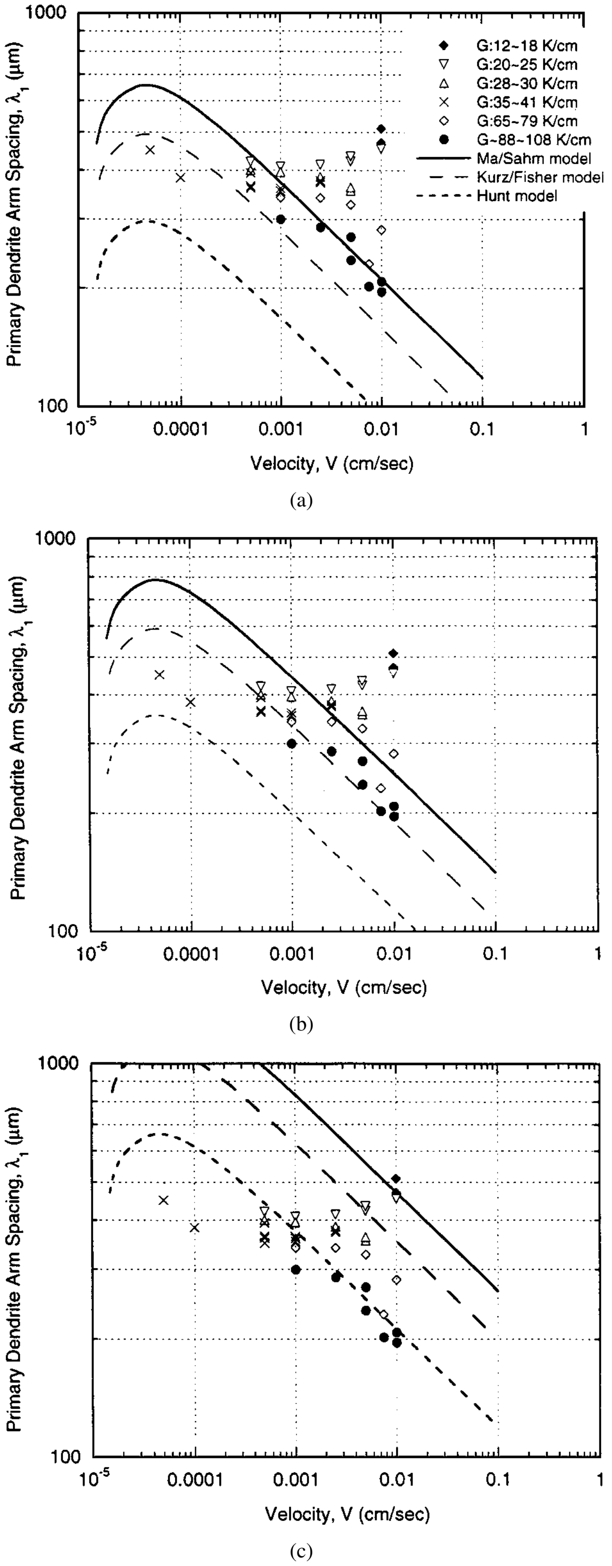

(a)

(b)

(c)

Figure 9 Comparison of the growth velocity dependence of the primary spacing of PWA1484 with theoretical predictions. (a) $G_{\text{theoretical}} = 100$ K/cm, (b) $G_{\text{theoretical}} = 70$ K/cm, and (c) $G_{\text{theoretical}} = 20$ K/cm.

a given solidification condition: one solution for dendritic growth with a larger value of λ_1 and (ii) another solution for cellular growth with a smaller value of λ_1. The samples grown at low velocities in the present experiments (i.e., 0.001 and 0.0005 cm/sec) typically exhibit flanged-cell microstructures (i.e., Figs 2c and 3c) for all investigated thermal gradients and the observed spacings are between the values predicted Lu and Hunt's numerical calculation for steady dendritic or cellular growth. Additional theoretical work is clearly needed to address the complex problem of mixed mode growth.

Fig. 10b also shows that very large dendritic spacings are predicted at low solidification velocities and low thermal gradients. Although not the focus of the present investigation, a superalloy 718 sample cylinder of diameter 0.6 cm and 5 cm length was previously frozen with approximate values of $V = 10^{-5}$ cm/s and $G \sim 1$°C/cm. Fig. 11 shows the tranverse microstructure of this sample. Although only a single primary dendrite developed, extensive secondary and tertiary arms are present. The secondary arm lengths grew as large as the sample macro-dimensions giving $\lambda_1 > 6000$ μm. This approximately agrees with Lu and Hunt's model which predicts $\lambda_1 \sim 10{,}000$ μm for such conditions.

3.3. Effects of off-axis heat flow

Grugel and Zhou [20] investigated the effects of off-axis heat flow on the primary dendrite spacings for succinonitrile-1.4 and 4.7 wt. pct. water alloys and found good empirical correlation between the spacings and the angular relationship between the dendrite growth direction and the total thermal gradient. Grugel and Zhou defined the orientation angle ϕ such that

$$\tan(\phi) = \frac{G_T}{G} \tag{9}$$

where G_T is the thermal gradient in the transverse direction and G is the thermal gradient in the longitudinal direction. These researchers found that the primary spacings increased with misalignment angle from 0–40° for constant conditions of composition, velocity, and thermal gradient. For increasing angles from 50–70°, the secondary arms assumed the roles of primaries and the spacings rapidly decreased. Grugel and Zhou correlated λ_1 with the heat flow geometry and found for the succinonitrile-1.4 wt. pct. water alloy that

$$\lambda_1(\phi) = \lambda_1(\phi = 0) + 120\tan^2\phi \cdot (\mu\mathrm{m}) \qquad (10)$$

where the 120 factor is an empirical fitting parameter. Thus the primary spacings of the samples in the misaligned thermal field were equal to the theoretical spacings during aligned growth ($\phi = 0$) plus a correction factor that depended upon the misalignment angle ϕ. Although the data were limited, Grugel and Zhou found a correction factor of approximately 260 $\tan^2\phi$ for misaligned growth in succinonitrile-4.7 wt. pet. water alloy. Thus the factor in front of the $\tan^2\phi$ term does not appear to be constant. More work on the basis of this factor is clearly needed.

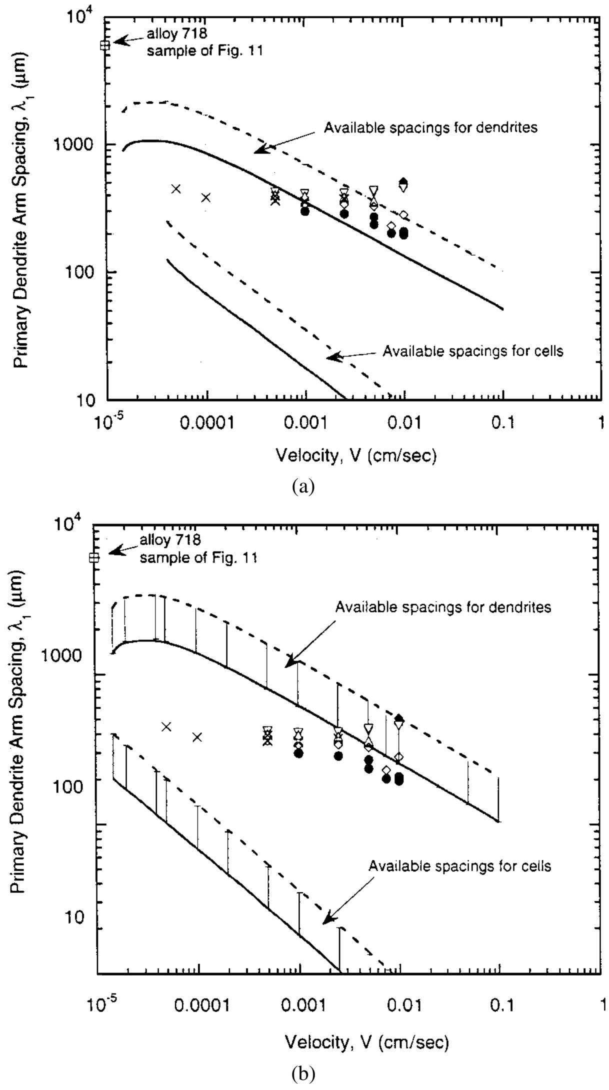

(a)

(b)

Figure 10 Comparison of the growth velocity dependence of the primary spacing of PWA1484 with theoretical predictions from numerical model of Lu and Hunt [14, 15]. $G_{\text{theoretical}} = 100$ K/cm, and (b) $G_{\text{theoretical}} = 20$ K/cm.

High growth velocities during directional solidification can move a sample's mushy zone down and out of the adiabatic zone, thus producing non-negligible transverse (i.e., radial) thermal gradients, especially when the axial thermal gradients being utilized are themselves quite low. An experiment was conducted to investigate the longitudinal (G) and radial (G_r) thermal gradients in the Bridgman-type furnace for a number of withdrawal velocities. Thermocouples were placed along the centerline and along the outside of samples. The test was performed with a furnace setting of 1200°C. Analysis of thermocouple data showed that when $G < 30$ K/cm, the ratio of radial to longitudinal thermal gradient (G_r/G) varied from 0.4, 0.3, and 0.2, respectively for velocities of 0.01, 0.005, 0.001 cm/sec.

Significant radial thermal gradients should increase the primary spacings along the outside edge of the samples. Fig. 12a shows the spacing distribution for a high velocity sample and a low velocity sample grown at low imposed gradient $G \sim 20$°C/cm. The measurements were performed along two mutually perpendicular diameters. The top two curves (diamonds) were measured on a sample grown at 0.01 cm/sec. The bottom two curves (triangles) represent the spacing distribution

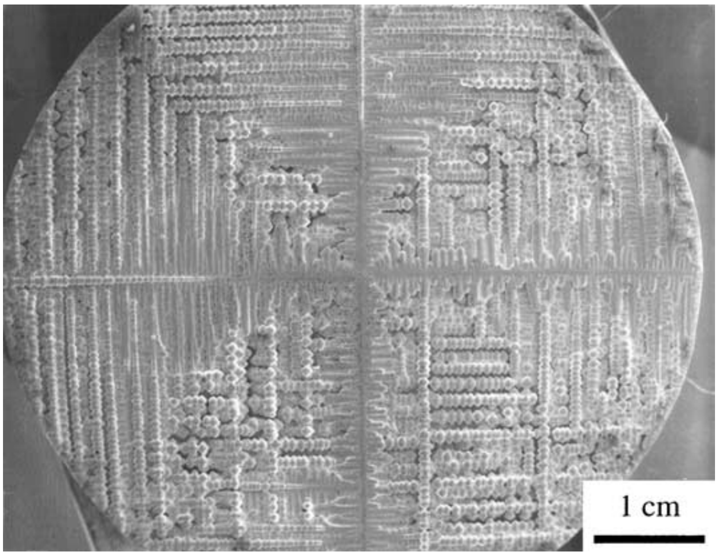

Figure 11 The top view of an as-cast single crystal nickel-based superalloy 718. Only one dendrite was formed in the sample. The length of the secondary arms was measured as the radius of sample (3 mm).

from a sample grown at 0.0005 cm/sec. The high velocity sample is expected to suffer the greatest radial thermal gradient and exhibits the greatest variation in primary dendrite arm spacing, as expected. The low velocity sample is expected to suffer the least radial thermal gradient and exhibits a quite uniform primary dendrite arm spacing. Fig. 12b shows additional spacing data including data from high G_L samples. At high G_L (>30°C/cm), the observed dendrite arm spacings were uniform.

Misalignment of growth direction and thermal gradient provides for enhanced growth of the secondary arms that find themselves rotated closer to the maximum thermal gradient.

Conversely, secondary arms on the opposite side will find their growth retarded since they are rotated away from the maximum thermal gradient. In the limit of a complete rotation through 90°, the secondary arms would obviously become primary arms. Such conditions could be realized by rapid withdrawal of a sample from the furnace followed by air cooling. Quantitative theoretical treatment of the effects of such misalignment would require numerical modeling the coupled solute/thermal diffusion fields at the dendrite tips.

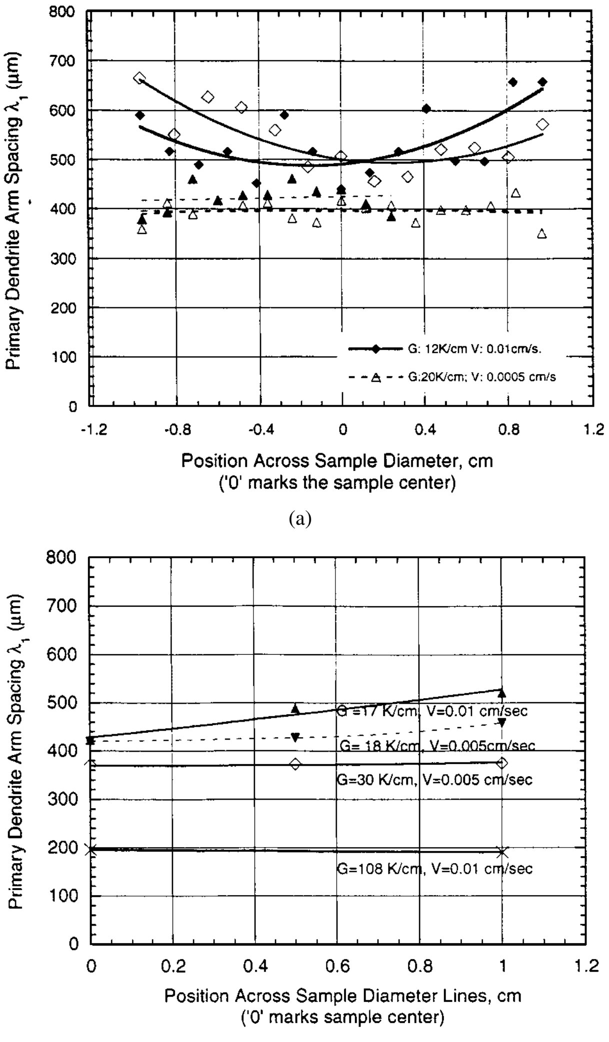

(a)

(b)

Figure 12 The variation of primary arm spacings across the diameter along two mutually perpendicular diameters. (a) Arm spacing distribution for samples grown at low gradient of ~20 K/cm. Diamonds represent data from sample grown at 0.01 cm/sec; triangles represent data from sample grown at 0.0005 cm/sec. and (b Arm spacings at center, middle and side of samples grown at 0.005 and 0.01 cm/sec under various gradients. Triangles represent samples grown at low gradients (17–18 K/cm); diamonds represent samples grown at medium-to-high gradients (28 K/cm and 105 K/cm).

4. Summary

Directional solidification experiments were performed on PWA1484, a complex multicomponent nickel-base superalloy. Solidification velocities were varied from 0.00005 to 0.01 cm/sec and thermal gradients varied from 12–108°C/cm. A range of aligned solidification microstructures were exhibited by the alloy when examined as-cast at room temperature: aligned dendrites with well developed secondary and tertiary arms; flanged cells aligned with the growth direction and without secondary arms; and cells with no evidence of flanges or secondary arms. Quenched directional solidification experiments indicated that although no secondary arms were present in the as-cast condition of flanged cell samples, secondary arms were present in the vicinity of the cell tips during solidification. Presumably coarsening phenomena eliminated the secondary arms during cooling through the mushy zone.

The well-known exponential equation ($\lambda_1 \propto G^{-1/2} V^{-1/4}$) describing primary arm spacing λ_1 with thermal gradient G and solidification velocity V exhibits excellent agreement with experimental data for PWA1484. However, the constant of proportionality is different depending upon whether the solidification microstructure contains secondary arms or not. The presence of secondary arms increases the spacing between dendrites and leads to a greater sensitivity of λ_1 on $G^{-1/2}\ V^{-1/4}$. When the secondary arms are not preserved in the room temperature microstructure, the primary spacings are much less sensitive to changes in the solidification parameter $G^{-1/2}\ V^{-1/4}$.

The PWA1484 multi-component alloy was assumed to act as a pseudo-binary alloy and the primary dendrite arm spacing results were compared to recent theoretical models proposed by Lu and Hunt [14, 15] and Ma and Sahm [16]. The models of Lu and Hunt and Ma and Sahm provided excellent agreement at medium to high thermal gradients and a wide range of solidification velocities. The experimentally determined exponent of V was shown to vary with the imposed thermal gradient. At high thermal gradients (88–108°C/cm), the exponent was measured as −0.19, approaching the theoretical value of −0.25. However, the useage of the pseudo-binary alloy approach and the difficulty in precision measurement of the various thermophysical parameters required for the theoretical estimates should caution readers against drawing firm conclusions about the specific validity of any specific theoretical model.

Finally, off axis heat flows were shown to cause radial non-uniformity in the dendrite arm spacing data for low thermal gradients and large withdrawal velocities.

Acknowledgments

This material is based upon work supported by, or in part by, the U.S. Army Research Office under grant number ARO DAAHO4-96-I-0321 and the National

Aeronautics and Space Administration under cooperative agreement number NCC8-128. The samples were graciously provided by Howmet Corporation, Whitehall, MI. Technical discussions and the assistance of Dr. Boyd Mueller and Mr. Terry Simon of Howmet Corporation in preparing the investment cast precursor bars are especially appreciated.

References

1. J. R. SARAZIN and A. HELLAWELL, *Metall. Trans.* **19A** (1988) 1861.
2. S. N. TEWARI and R. SHAH, *Metall. Mater. Trans.* **27A** (1996) 1353.
3. T. M. POLLOCK and W. H. MURPHY, *ibid.* **27A** (1996) 1081.
4. S. H. HAN and R. TRIVEDI, *Acta Metall. Mater.* **42** (1994) 25.
5. H. K. KIM, J. C. EARTHMAN and E. J. LAVERNIA, *ibid.* **40** (1992) 637.
6. M. VIJAYAKUMAR and S. N. TEWARI, *Mater. Sci. and Eng.* A **132** (1991) 195.
7. M. A. CHOPRA and S. N. TEWARI, *Metall. Trans.* **22A** (1991) 2467.
8. D. BOUCHARD and J. S. KIRKALDY, *Metall. Mater. Trans.* **28B** (1997) 651.
9. K. SOMBOONSUK, J. T. MASON and R. TRIVEDI, *Metall. Trans.* **15A** (1984) 967.
10. R. TRIVEDI, *ibid.* **15A** (1984) 977.
11. J. D. HUNT, in "Solidification and Casting of Metals" (The Metals Society, London, 1979) p. 3.
12. W. KURZ and D. J. FISHER, *Acta Metallurgica* **29** (1981) 11.
13. J. S. LANGER and H. MULLER-KRUMBHAAR, *J. Crystal Growth* **42** (1977) 11.
14. J. D. HUNT and S. Z. LU, *Metall. Trans.* **27A** (1996) 611.
15. S. Z. LU and J. D. HUNT, *J. Crystal Growth* **123** (1992) 17.
16. D. MA and P. SAHM, *Metall. Mater. Trans.* **29A** (1998) 1113.
17. M. B. ESHELMAN, V. SEETHARAMAN and R. TRIVEDI, *Acta Metall. Mater.* **36** (1988) 1165.
18. R. J. SU, R. A. OVERFELT and W. A. JEMIAN, *Metall. Mater. Trans.* **29A** (1998) 2375.
19. R. J. SU, W. A. JEMIAN and R. A. OVERFELT, *J. Crystal Growth* **179** (1997) 625.
20. R. N. GRUGEL and Y. ZHOU, *Metall. Trans.* **20A** (1989) 969.
21. M. C. FLEMINGS in "Solidification Processing" (McGraw-Hill Inc., New York, 1974) p. 66.
22. W. KURZ and D. J. FISHER, in "Fundamentals of Solidification" (Trans Tech Publications, Aedermannsdorf, Switzerland, 1992) p. 65.
23. D. G. McCARTNEY and J. D. HUNT, *Acta Metallurgica* **29** (1981) 1851.
24. D. MA and P. R. SAHM, *Z. Metallkd.* **82** (1990) 869.
25. L. BACKERUD, G. CHAI and J. TAMMINEN, in "Solidification Characteristics of Aluminum Alloys, Vol 1: Wrought Alloys" (AFS/Skanaluminium, Des Plaines, IL, 1990) p. 65.
26. J. LAPIN, A. KLIMOVA, R. VELISEK and M. KURSA, *Scripta Materialia* **37** (1997) 85.

Received 8 March 2001
and accepted 5 April 2002